An LFM-Based Semiblind Synchronization Method for Bistatic Radar Imaging

James Park, *Member, IEEE*, and Raghu G. Raj, *Senior Member, IEEE*

***Abstract*—Bistatic radar provides an additional degree of freedom in the observing geometry for imaging by using a spatially separated transmitter and receiver. This capability allows the capture of scattering phenomena at various bistatic sensing angles, which helps to interpret the physical characteristics of a target or scene for remote sensing and radar applications. A crucial problem associated with bistatic radar is the synchronization of time and frequency between the transmitter and receiver for coherent image formation. In this article, a model-based method of synchronization, called semiblind synchronization, is introduced for maintaining the phase coherence of a bistatic radar system for range-Doppler processing. Specifically, semiblind synchronization refers to bistatic synchronization where the direct path is not available or where the global positioning system signal is not accurate enough, and where prior knowledge of the transmit waveform and target location are exploited during a coherent processing interval. The method focuses on error estimation and compensation based on understanding the impact of synchronization errors on the received signals. After detailing our system model and semiblind synchronization method, we conduct a simulation study for assessing the effectiveness of our method by first introducing a variety of synchronization errors, including chirp rate mismatch, and time and frequency offsets. Scattering responses from a point target are simulated, and high-range resolution profiles and range-Doppler images are formed to validate the proposed method. The simulation results demonstrate that a linear frequency modulation waveform enables us to estimate and compensate the synchronization errors considered in this article and improve the overall quality of the bistatic range-Doppler image. Our synchronization technique has potentially broad applicability in emerging remote sensing applications using bistatic radar systems.**

***Index Terms*—Bistatic radar, range-Doppler processing, stretch processing, synchronization.**

I. Introduction

RADAR images are used in a variety of remote sensing applications for detecting and monitoring the physical characteristics of an area, such as from satellites or aircraft. In recent years, bistatic imaging systems have been actively proposed and discussed in radar and remote sensing communities because of their various advantages [1], [2], [3], [4], [5], [6], [7], [8], [9], [10], [11], [12], [13], [14], [15]. For example, unlike traditional monostatic systems, bistatic radar systems have separated transmitters and receivers at different locations, introducing an additional degree of freedom in the observing geometry. This ability allows the systems to capture the scattering features from radar images in bistatic geometries, which provide further information to understand the physical properties of a scene that consists of both natural and man-made structures.

To form bistatic radar images, synchronization with respect to frequency and time must be achieved between the spatially separated transmitter and receiver [2], [3], [4], [5], [6], [7], [8], [9], [10], [11], [12], [13], [14], [15]. The oscillator noise, including frequency offset and phase noise, causes a time-variant shift, spurious sidelobes, and a Doppler widening of the radar response on the resulting bistatic synthetic aperture radar (SAR) and inverse SAR (ISAR) images, as reported in [2], [3], [4], [5], [6], [7], [8], [9], [10], [11], [12], [13], [14], and [15]. The most common approaches to synchronize bistatic radar are using high-precision oscillators, such as chip-scale atomic clocks and global positioning system disciplined oscillators (GPSDOs), in conjunction with direct-path signals, synchronization links, or GPS time.

For example, in [8], the direct-path signal from transmitter to receiver is used for synchronization for bistatic SAR imaging. The direct-path signals are first used to synchronize sampling clock and phase errors on the receiver end, and then the residual time and phase errors are compensated with GPS or inertial navigation system or inertial measurement unit information. Furthermore, synchronization using a long round-trip fiber optic link was proposed to cancel the effective phase error for ground-based bistatic ISAR images without GPS timing information in [9].

A synchronization link, which is also known as two-way time transfer synchronization, is widely used to exchange the oscillator signals between transmitter and receiver for space-borne bistatic SAR imaging [2], [10], [11], [12]. Synchronization signals are exchanged between the satellites and then, by adequate signal processing, the phase errors and drifts caused by oscillators are corrected for bistatic SAR signals. Additionally, modern communication and software-defined radio (SDR) technologies allow for the synchronization of distributed sensors via wireless sensor networks (WSNs) [2], [11]. Using WSNs, < 50 ps precision among three SDR-based radar systems was demonstrated in [11].

Synchronization methods leveraging high-precision oscillators and pulse-per-second (PPS) signals have been investigated

Manuscript received 17 June 2024; revised 29 July 2024; accepted 30 July 2024. Date of publication 14 August 2024; date of current version 5 September 2024. This work was supported by the Office of Naval Research through the Naval Research Laboratory Base Program. *(Corresponding author: James Park.)*

The authors are with the Radar Division, U.S. Naval Research Laboratory, Washington, DC 20375 USA (e-mail: james.park16.civ@us.navy.mil; raghu.g.raj.civ@us.navy.mil).

Digital Object Identifier 10.1109/JSTARS.2024.3443547

in [13], [14], and [15]. To achieve the required time and phase precision for distributed SAR, GPS time information and PPS signals are used with range alignment and subaperture autofocus algorithms, which compensate the residual phase errors in [13]. Additionally, in [15], three independent radar systems were synchronized by allowing a common PPS signal to pass at all nodes. A low jitter trigger signal was derived from the synchronous PPS output of the GPSDOs. The performance of various commercial-off-the-shelf (COTS) devices was characterized to develop the GPS-based radar synchronization systems.

Although synchronization approaches for bistatic SAR and ISAR imaging have been reported in the literature, to the best of our knowledge, a synchronization method for enabling radar imaging, where a direct path or GPS is not available, has not been explored. In this article, we present a novel model-based synchronization methodology that we call semiblind synchronization for overcoming this problem. In particular, we develop a linear frequency modulation (LFM) based semiblind synchronization method, which estimates and compensates synchronization errors based on the knowledge of the contribution of those errors on received signals. Our analysis focuses on understanding the contribution of synchronization errors on phase errors of the received signals through bistatic stretch processing [6], [16]. Synchronization errors, including chirp rate mismatch, and time and frequency offsets, are considered in bistatic stretch processing on the receiver chain. There has been little to no published work on stretch processing for bistatic high-range resolution profiles (HRRP), and range-Doppler and ISAR imaging to address synchronization-induced phase errors. The proposed method does not require an exchange of oscillator signals between the transmitter and receiver or direct-path signals, but prior knowledge of the transmit LFM waveform and target location, and is agnostic to whether the scene contains natural or man-made structures. Our synchronization techniques impact a wide range of bistatic imaging scenarios in support of large-scale Earth observations via remote sensing systems.

The rest of this article is organized as follows. Section II introduces the bistatic radar system model using stretch processing. Synchronization errors and simulation parameters are also discussed in this section. The impact of synchronization errors on range-Doppler processing and resulting images is then presented in Section III. Section IV introduces the LFM-based, semiblind synchronization method and provides proof-of-concept using simulation. Finally, Section V concludes this article.

II. System Model

A bistatic system consists of a transmitter and receiver mounted on different platforms separated in time and space and each with an independent oscillator. In this section, a bistatic radar imaging system using stretch processing is discussed with a focus on synchronization errors. In the bistatic radar system model using stretch processing, an LFM pulse waveform is considered. The LFM pulse waveform is first generated from a waveform generator at baseband, and then the baseband waveform is upconverted to the center radio frequency (RF) Ω_T by mixing the output of a phase-locked loop (PLL) local oscillator (LO) centered at frequency Ω_o. During upconversion, errors in frequency offset $\Delta\ \Omega_T = \Omega_T\ - \Omega_o$ and transmitter phase noise φ_T occur depending on the accuracy and stability of the PLL and LO. The RF waveform goes through a power amplifier and a transmitting antenna, as shown in Fig. 1. The returned signals from scatterers after a low-noise amplifier are expressed as

$$\tilde{x}_k\ (t) = \sum_{i=1}^{N} \xi_i \exp\left(j\frac{\pi\beta}{\tau}(t-t_{b_i})^2\right) \exp\left(j\left[\Omega_T\,(t-t_{b_i}) + \varphi_T\,(t-t_{b_i})\right]\right),\ 0 \le t - t_b \le \tau \tag{1}$$

where N is the number of scatterers, β is the chirp rate, ξ is the reflectivity of scatterers, τ is the pulsewidth, k is the pulse number, Ω_T is the carrier frequency with frequency offset on transmitter, φ_T is the transmitter phase noise, and t_b is the time delay associated with distance R_b from the transmitter to the scatterer and to the receiver, as shown in Fig. 1. In Fig. 1, both the standard clean received signal (in blue font) and the synchronization error parameters in the transmitter and receiver (in red font) have been highlighted.

A. Synchronization Error Parameters

In bistatic radar, there are three types of clock jitter that contribute to synchronization errors of the received signal: frequency offset, time offset, and chirp rate mismatch. Frequency offset $\Delta\Omega$ is the frequency difference between output signals from the transmitter's and receiver's PLLs and LOs that deviate from the carrier frequency. The time synchronization determines the accuracy of the range measurement. A typical requirement for time synchronization is about one-tenth of the compressed pulsewidth [2]. The GPSDO provides $\sim$10 ns accuracy relative to UTC [11], [13]. A significant source of error in time synchronization of the precisely calibrated GPSDO COTS equipment is the biasing of the GPS receiver. The time accuracy of received PPS signals depends on the precision of the timestamp, which, in turn, can be significantly affected by the accelerated motion of the receiver platform. Chirp rate mismatch α may occur in stretch processing on the bistatic receiver as introduced in (2). The output of the stretch processing removes the carrier frequency from the received echo and combines it in a mixer with a replica of the transmitted LFM waveform with a delay corresponding to the central reference point (CRP). Since bistatic radar consists of a separated transmitter and receiver using independent up and down converters, the received echo can be mixed with an LFM signal with a different chirp rate causing distortion of the output signal [6].

B. Stretch Processing-Based Synchronization Error Analysis

Stretch processing reduces the bandwidth requirement that must be satisfied by the receiver and processor [6], [16], [17], [18], and it facilitates ultrawideband imaging applications, which provide high down-range resolution. At the receiver,

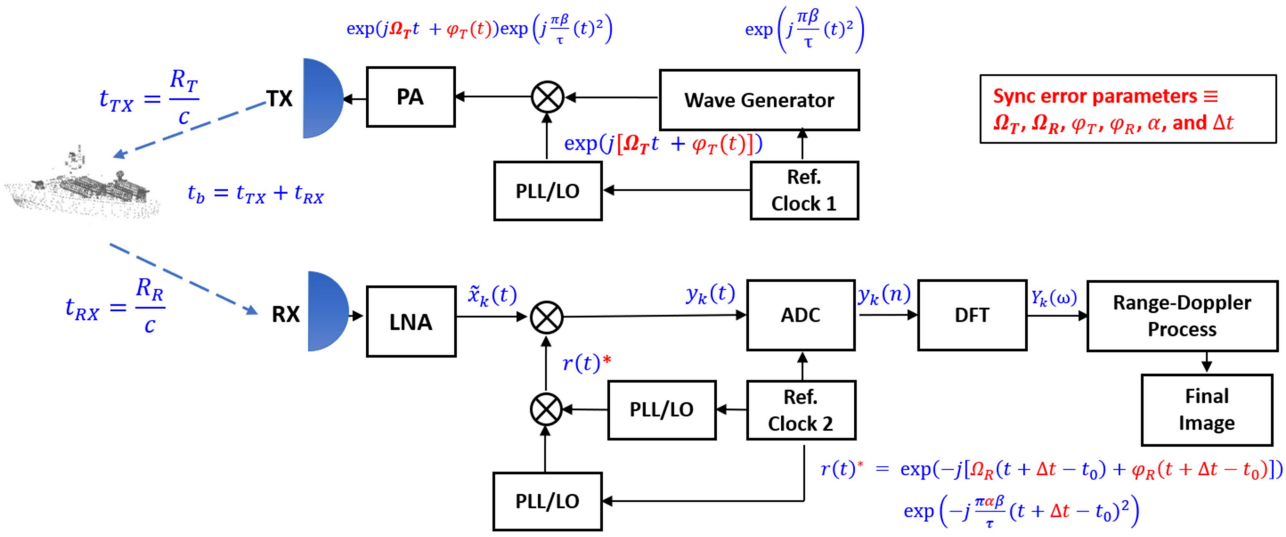

Fig. 1. Bistatic system model using stretch processing.

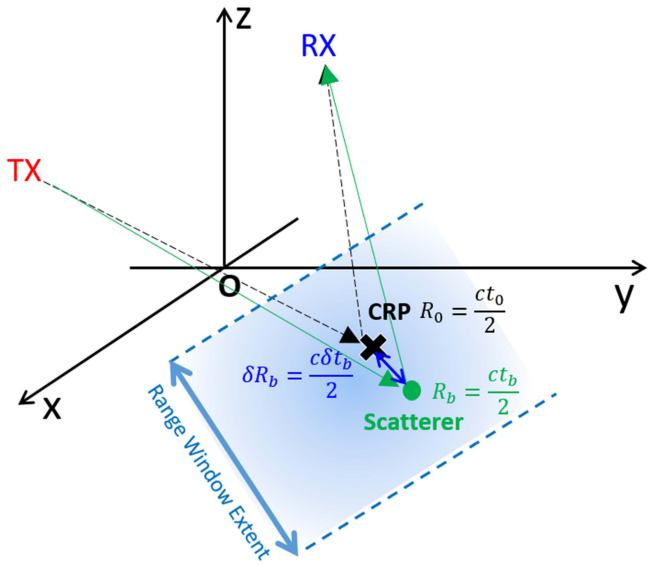

Fig. 2. Scenario for stretch processing in bistatic radar.

stretch processing is considered in the system model. Fig. 2 shows the scenario for stretch processing in bistatic radar. The CRP is at the middle of the range window extent at R_0 corresponding to a time delay of t_0. The differential time delay and range relative to the CRP are denoted as ΔR_b and Δt_b, respectively [18].

Stretch processing consists of deramp processing and pulse compression using a Fourier transform. The Fourier transform performs a spectral analysis of the mixer output signal. The synchronization errors occur in the down-conversion and deramp processing before the analog-to-digital converter (ADC) and the discrete Fourier transform (DFT) block. The stretch processing is done by mixing (1) with the reference signal from the receiver's PLL and LO and an arbitrary waveform generator.

The reference signal is

$$r(t) = \exp\left(-j\left[\Omega_R(t + \Delta t - t_0) + \varphi_R(t + \Delta t - t_0)\right]\right) \exp\left(-j\frac{\pi\alpha\beta}{\tau}(t + \Delta t - t_0)^2\right) \tag{2}$$

where $\Omega_R = \Omega_o + \Delta\Omega_R$ is the down-conversion frequency with receiver frequency offset $\Delta\Omega_R$, φ_R is the receiver phase noise, Δt is the time offset, and α is the chirp rate mismatch factor. Note, (2) contains Ω_R to remove the carrier and a replica of the transmitted chirp rate β referenced to the time delay t_0. After the mixer, the received signal y is expressed as follows:

$$y_k(u) = \exp\left(-j\phi_\varepsilon(u)\right) \sum_{i=1}^{N} \xi_i \exp\left(j\phi_{b_i}(u)\right), \; u = t + \Delta t. \tag{3}$$

The fast time t with time offset Δt on the receiver chain is substituted to u. In (3), the phase error $\phi_\varepsilon(u)$ due to the contribution of synchronization errors is

$$\begin{aligned}\phi_\varepsilon(u) &= \left[\frac{\pi\beta}{\tau}\Delta t - (\Omega_0 + \Delta\Omega_T)\right]\Delta t \\ &\quad - \left[\frac{2\pi\beta}{\tau}\Delta t + (\Delta\Omega_R - \Delta\Omega_T)\right](u - t_0) \\ &\quad + \frac{\pi\beta}{\tau}(1 - \alpha)(u - t_0)^2 + \varphi_R(u - t_0) \\ &= \mathcal{C}_0 + \mathcal{C}_1(u - t_0) + \mathcal{C}_2(u - t_0)^2 + \varphi_R(u - t_0).\end{aligned} \tag{4}$$

Our analysis shows that the phase error is expressed as a quadratic function

$$\mathcal{C}_0 = \left[\frac{\pi\beta}{\tau}\Delta t - (\Omega_0 + \Delta\Omega_T)\right]\Delta t \tag{4.1}$$

$$\mathcal{C}_1 = -\left[\frac{2\pi\beta}{\tau}\Delta t + (\Delta\Omega_R - \Delta\Omega_T)\right] \tag{4.2}$$

$$\mathcal{C}_2 = \frac{\pi\beta}{\tau}\,(1-\alpha)\,. \tag{4.3}$$

Note that the transmitter frequency offset $\Delta\Omega_T$ and time offset Δt contribute to both C_0 and C_1, while chirp rate mismatch α only contributes to C_2. It is assumed that, in this study, $\Delta\Omega_T$ is unknown, but $\Delta\Omega_R$ can be measured on the receiver. The phase contribution of scattering response $\phi_{b_i}(t)$ as a function of fast time t is

$$\phi_{b_i}\ (t) = -\frac{2\pi\beta}{\tau}\Delta t_{b_i} t - \theta \tag{5}$$

where $\theta\ = ((\Omega_0 + \Delta\Omega_T) - \frac{2\pi\beta}{\tau}t_0)\ \Delta t_{b_i} + \frac{\pi\beta}{\tau}(\Delta t_{b_i}\ )^2$. The derivation of (4) and (5) for the received signal is provided in the Appendix.

In the system model, the received signal in (5) is sampled via ADC, which produces

$$\begin{aligned} y\,(n)\ &= \exp\left(j\left(\frac{2\pi\beta}{\tau}\Delta t_b\,(nT_s) - \theta\right)\right)\ n \\ &= 0,\ 1, \ldots,\ (N_s - 1) \end{aligned} \tag{6}$$

where T_s is the ADC sampling period $F_s = 1/T_s$. The DFT is applied to the received signal in (6). A fast Fourier transform (FFT) can be considered for the DFT to efficiently generate the HRRP. The DFT is defined as

$$\begin{aligned} Y\ (m)\ &= \sum_{n=0}^{N_s-1} y\,(n)\ \exp\left(-j2\pi\frac{nm}{M}\right)\ m \\ &= 0,\ 1,\ \ldots,\ (M-1) \end{aligned} \tag{7}$$

where M is the total sample number of range cells. The DFT of (6) is expressed as

$$|Y\,(m)| = \left|\frac{\sin\left(\frac{N}{2}\left(\frac{2\pi m}{M} - \frac{2\pi}{F_s}\frac{\beta\Delta t_b}{\tau}\right)\right)}{\sin\left(\frac{1}{2}\left(\frac{2\pi m}{M} - \frac{2\pi}{F_s}\frac{\beta\Delta t_b}{\tau}\right)\right)}\right|\,. \tag{8}$$

Equation (8) is the compressed range response associated with a scatterer. In the range response, a scatterer is located at the mth DFT bin related to time delay $\Delta t_b = \frac{F_s\tau m}{\beta M}$. The width of the main lobe of (8) determines the range resolution [19]. Through the stretch processing, the HRRPs $Y_k(m)$ are collected in dwell time and sent to the range-Doppler processing block.

C. Range-Doppler Simulation

We first simulated the returned signals from a point-scatter model using the system model without synchronization errors, as discussed in Section II-A. The point-scatter model consisted of 9774 3-D scatterers representing a boat, as shown in Fig. 3. The size of this boat is ∼116 m long and ∼24 m wide. The highest and the lowest point scatterers are located at z =∼34 m and z =∼−12 m. The carrier frequency was set to 9.5 GHz, and the chirp bandwidth β and pulsewidth τ of the LFM waveform were fixed to 500 MHz and 1 μs, respectively. A pulse repetition interval (PRI) of 0.5 ms, which is consistent with 2 kHz pulse repetition frequency, and a sample rate of 2 GHz were selected in this simulation study.

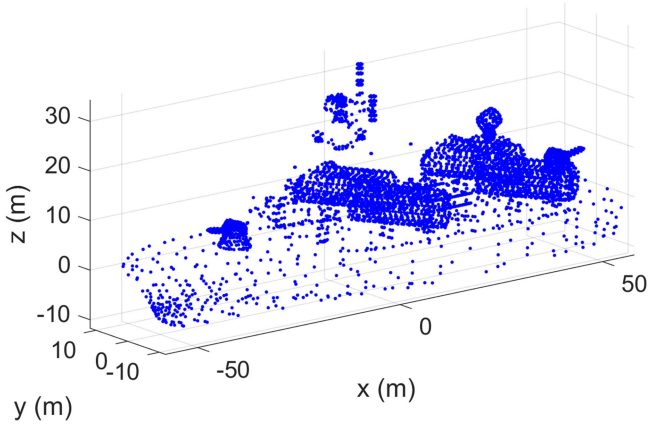

Fig. 3. Three-dimensional point scatterers representing a boat.

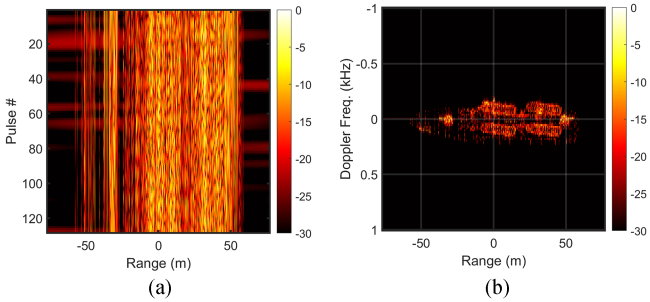

Fig. 4. Simulation of (a) range profiles and (b) resulting range-Doppler image without synchronization errors.

The range-Doppler and ISAR imaging process leverages Doppler shifts induced by the rotational motion of a target. A target can be rotated about three orthogonal axes: yaw ψ, roll ϕ, and pitch θ. The rotation angle is modeled as

$$\psi/\phi/\theta\,(k) = C \times \text{PRI} \times k + M\sin\left(\frac{2\pi \times \text{PRI} \times k}{P}\right) \tag{9}$$

where C is the constant rate (°/s), M is the sinusoid magnitude (°), and P is the parameter for the sinusoid period (s). Nominal rotation angle for a boat was modeled as $C = 5$ and $P = 1$ for ψ, and $M = -5$ and $P = 10$ for θ. The rotation angle varies as a function of pulse number k during the coherent processing interval (CPI) time. Note that the translational motion of a target was not considered in this simulation to focus on the assessment of synchronization errors.

After pulse compression through stretch processing, the baseband in-phase (I) and quadrature (Q) data collected in CPI time are organized into an $M \times K$ complex matrix for range-Doppler imaging. The complex matrix consists of K range profiles where each range profile has M range cells. The HRRP represents the energy distribution of the received signal as a function of range. Magnitude peaks of the HRRP indicate the range locations of dominant scatterers. In an HRRP, if one or more magnitude peaks are detected at certain range cells, it indicates that one or more dominant scatterers have been detected at the corresponding locations. Fig. 4(a) shows the HRRPs, $G(r_m, t_k)$, consisting

of $K = 128$ pulses using the simulation parameters and rotation angle. Note that t_k is the time series over the CPI time, and r_m is the fast time (slant range) samples.

The Fourier image formation takes the Fourier transform at each range cell along K pulses and generates a Doppler spectrum called the Doppler profile. Since the translational motion is not considered in the simulation, a motion compensation algorithm is not applied to the imaging process. Finally, by adjoining the Doppler spectra for each of the M range cells, the $M \times K$ range-Doppler image is formed as follows:

$$I\ (r_m, f_k) = \mathrm{FFT}_k\ \{G\,(r_m, t_k)\}\,. \tag{10}$$

Note that f_k is the Doppler sample after FFT. Fig. 4(b) shows the resulting range-Doppler image generated from the HRRPs in Fig. 4(a). The horizontal and vertical axes of the range-Doppler image represent the slant range and Doppler frequency, respectively. Each image is normalized by its maximum intensity. The simulation results show that, without synchronization errors, the scattering responses from the boat's structure are well focused on the range-Doppler image in this case.

III. Impact of Synchronization Errors on Range-Doppler Image

We are now in a position to define the specific models for each of the synchronization error parameters, including the frequency offset, the time offset, and the chirp mismatch in our bistatic system setup described in Section II; this is explicated in Section III-A. We found that the phase difference has a negligible impact on image quality based on the simulation study, so this error is not focused on this article. Thereafter, we explore the impact of the synchronization error parameters on range-Doppler imaging in Section III-B. We have investigated the impact of the phase difference on image qualitatively. However, its impact was minor based on simulation. Thus, the phase difference is not focused in this article.

A. Synchronization Errors' Models

We consider the scenario where the bistatic radar does not share an oscillator between transmitter and receiver chains, which causes frequency and time offsets. Those offsets are one of the sources of synchronization errors. An oscillator's frequency and time may drift or vary in time depending on environmental effects, such as temperature, acceleration (gravity and vibration), power supply voltage, and atmospheric pressure [21].

The CPI for range-Doppler and ISAR imaging is typically less than 1 s. In this case, transmitter frequency offset is modeled using three parameters as follows:

$$\Delta\Omega_T\ (k) = \eta_0\ + \eta_1 k + n_\Omega\,(k) \tag{11}$$

where η_0 is the initial frequency offset and η_1 is the linear drift, which usually depends on the oscillator temperature and acceleration, and $n_\Omega(k)$ is the random jitter. The random jitter is usually much smaller than the initial offset and linear drift [4]. Constant frequency offset η_0 produces displacement in the image but no defocusing, but linear frequency drift η_1 dominantly causes defocusing in the Doppler direction, and random noise n_Ω increases the sidelobe levels. In a semiblind scenario, it is assumed that the bistatic radar system is synchronized at the beginning of the data collection, so the linear drift is focused on an error model in this article. Also, the receiver frequency offset $\Delta\Omega_R$ is assumed to be measured on the receiver end. Similar to the frequency offset, the time offset Δt is also modeled as follows:

$$\Delta t\ (k) = \gamma_0\ + \gamma_1 k + n_t\,(k)\,. \tag{12}$$

Similar to the frequency offset, the time variation of a clock generally depends on three independent components: initial clock offset γ_0, clock drift γ_1, and random additive noise n_t [22].

Additionally, in practice, the transmitter and receiver hardware and the atmosphere modify the magnitude and phase response of the waveform prior to the deramp processing [17], which can cause some changes in chirp rate β and pulsewidth τ. The contribution of these errors is captured in the chirp mismatch parameter α. The phase difference φ between the transmitter and receiver oscillators may increase the noise level of the received signal, but our analysis found that its impact on the image quality was negligible. Also, the initial frequency η_0 and time offsets γ_0 are constant in time and the random jitters $n_{\Omega/t}$ are very small values. Thus, the remainder of this article is focused on chirp rate mismatch, transmitter frequency drift, and time drifts.

B. Impact of Synchronization Errors on Range-Doppler Images

Synchronization errors, as discussed in Section III-A, are added to the system model to assess the impact of those errors on the range profiles and range-Doppler images. Fig. 5 shows a few examples, which demonstrate the negative impacts of various synchronization errors on image quality. These time-varying scattering responses were generated using the simulation parameters and rotational motion, as discussed in Section II-B. Each image was normalized by its own maximum intensity value.

Fig. 5(a) is an example showing range profiles (top) and range-Doppler images (bottom) where the transmitter frequency offset $\Delta\Omega_T$ drifts $\eta_1 = 100$ kHz every 0.5 ms PRI. Note that the nominal frequency drift η_1 is added to the system to observe its impact on the image quality. In this case, the phase error becomes $\phi_{\varepsilon,k}\,(t) = \mathcal{C}_1\,(t - t_0)$, where $\mathcal{C}_1 = \Delta\Omega_T\ = \eta_1\,k$. The contribution of frequency drift affects θ in (5), which becomes a function of k. A discrete-time Fourier transform of (5) along the pulses at the given range cell is

$$\begin{aligned} f_{D_i}\ (\omega)\ &= \sum_{k=0}^{K-1} \exp\left(j\Delta\Omega_T \Delta t_b\ \right) \exp\left(-j\omega k\right) \\ &= \sum_{k=0}^{K-1} \exp\left(j\eta_1 \Delta t_b k\ \right) \exp\left(-j\omega k\right) \\ &= \sum_{k=0}^{K-1} \exp\left(j(\eta_1 \Delta t_{b_i} - \omega)k\right). \end{aligned} \tag{13}$$

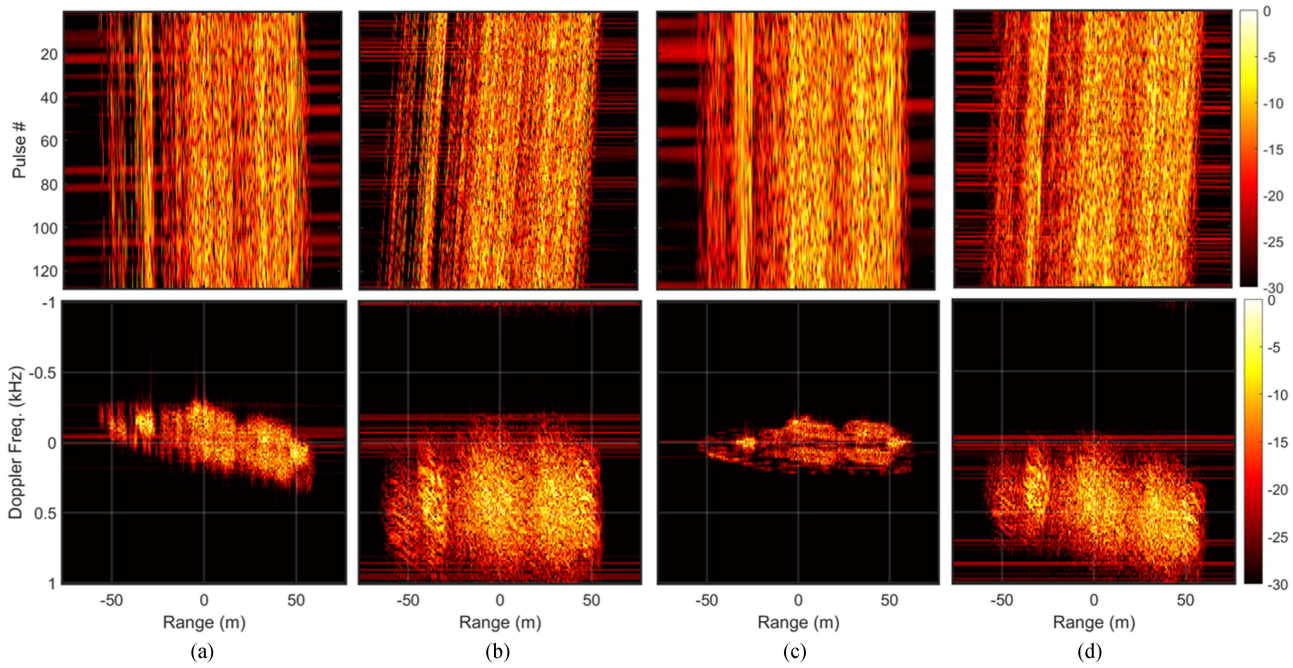

Fig. 5. Range profiles (top) and range-Doppler images (bottom) with (a) $\eta_1 = 100\,\text{kHz}$, (b) $\gamma_1 = 1\,\text{ns}$, (c) $\alpha = 0.9$, and (d) multiple synchronization errors considered in (a–c).

Equation (13) indicates that the Doppler shift of scatterer i varies depending on Δt_{b_i}, and the differential time delay determined by the scatterer's range relative to the CRP. Thus, the effect of linear frequency drift is that of shifting scattering centers along the Doppler coordinate, which appears as the scatterers are rotated in the range-Doppler image. The transmitter frequency drift also causes migration of scattering responses. Without compensating the frequency offset, the comparison of the range-Doppler images between Figs. 4(b) and 5(a) clearly shows that the image becomes smeared.

Fig. 5(b) shows the negative effects of time offset on the receiver chain and resulting images. The time offset is modeled as $\gamma_1 = 1\,\text{ns}$, which means that the time offset drifts 1 ns in fast time every 0.5 ms PRI. The phase error in this example is modeled as $\phi_{\varepsilon,k}(t+\gamma_1 k) = \mathcal{C}_0 + \mathcal{C}_1(t+\gamma_1 k - t_0)$, where $\mathcal{C}_0 = (\frac{\pi\beta}{\tau}\gamma_1 k - \Omega_0)\,\gamma_1 k$ and $\mathcal{C}_1 = -\frac{2\pi\beta}{\tau}\gamma_1 k$. The range profiles in Fig. 5(b) top show that the scattering peaks in the range profiles are shifted in fast time and range due to the time drift during the CPI time. The corresponding range-Doppler image looks blurry compared with Fig. 4(b) due to the linear time drift.

Fig. 5(c) is an example of range-Doppler processing where chirp rate mismatch occurs on stretch processing. The chirp mismatch parameter of $\alpha = 0.9$ is added in (4), which is $\phi_\varepsilon\,(t) = \mathcal{C}_2\,(t - t_0)$, where $\mathcal{C}_2 = \frac{\pi\beta}{\tau}\,(1-\alpha)$. Note that this chirp mismatch parameter is nominal. Since, in this example, the chirp mismatch parameter does not vary in slow time, the error only affects range responses. The mismatch error extends the scattering centers in the range cells, which results in poor resolution and overlap of adjacent scattering responses. The comparison of Figs. 4(b) and 5(c) shows that the mismatch degrades the down-range resolution and extends the scattering responses along the slant range as a result of distortion in the deramp processing.

In the last example, all three synchronization errors $\eta_1 = 100\,\text{kHz}$, $\gamma_1 = 1\,\text{ns}$, and $\alpha = 0.9$ are considered. Fig. 5(d) shows the resulting range profiles and range-Doppler image. The images show that the impact of the three errors is superposed into the phase error and significantly decreases the resulting image quality. These simulated I and Q data are used for testing the LFM-based, semiblind synchronization method in Section IV.

IV. LFM-Based Semiblind Synchronization Method

Our core, model-based, synchronization method, called semiblind synchronization, which builds upon the system model described in the previous sections, is explicated in Section IV-A. The image quality metrics used by our algorithm are described in Section IV-B. Finally, extensive simulation results validating our model-based synchronization technique are shown in Section IV-C. It is worth noting that the demonstration of the performance of our semiblind synchronization method on basic point targets and extended structures in Section IV-C points to the generality of our approach, which is applicable to general radar image data obtained from bistatic sensors in a variety of remote sensing applications.

A. Semiblind Synchronization Algorithm

Fig. 6 shows the block diagram of the LFM-based, semiblind synchronization method. The algorithm estimates synchronization errors via parametric sweep and image quality assessment (IQA) based on the knowledge of the structure of the transmitted waveform and received signal, as discussed in Section III. The

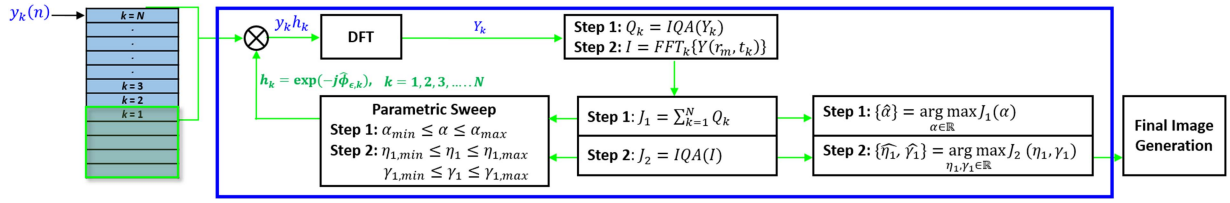

Fig. 6. Semiblind synchronization method using parametric sweep and IQA on the receiver.

quality of the range-Doppler image is quantitatively measured using methods to analyze the distortions and degradations due to synchronization errors added in the received signals. The image quality metrics are discussed in Section IV-B.

The semiblind synchronization method consists of two steps for error estimation. In Step 1, the chirp rate mismatch parameter α is estimated using (4.3). Among the three synchronization errors considered in this study, α only contributes to (4.3). The collected received signals y_k after the ADC are multiplied by the error compensation term h_k for given α. The error compensation term is

$$h_k = \exp(-j\hat{\phi}_{\epsilon,k}),\ k = 0,\ 1,\ 2,\ \ldots,\ (K-1) \tag{14}$$

where $\phi_{\epsilon,k}(t_k) = \mathcal{C}_2\, {t_k}^2$ and $\mathcal{C}_2 = \frac{\pi\beta}{\tau}(1-\alpha)$ in this case. This signal $y_k h_k$ is transformed to spectrum Y_k via the DFT block. The spectrum provides a range profile as the result of stretch processing. The quantitative quality values of range profiles for K number of pulses are computed using image quality metrics and the values are summed as

$$J_1\ (\alpha) = \sum_{k=0}^{K-1} \mathrm{IQA}\left(\hat{Y}_k\right). \tag{15}$$

The summation of the quality values J_1 is calculated, while α is varied from $\alpha_{\min}$ to $\alpha_{\max}$, as shown in the parametric sweep block in Fig. 6. The chirp rate mismatch parameter α is estimated by finding the maximum (best quality) value from J_1 as

$$\{\hat{\alpha}\} = \underset{\alpha \in \mathbb{R}}{\arg\max}\ J_1(\alpha). \tag{16}$$

Step 2 estimates the remaining error parameters, which are frequency drift η_1 and time drift γ_1 in conjunction with $\hat{\alpha}$ from Step 1. The phase contribution of all the synchronization errors in (4) is considered in Step 2. The frequency and time drifts are modeled as $\Delta\,\Omega_T = \eta_1\ k$ and $\Delta t\ = \gamma_1\ k$, respectively, and applied to (4.1) and (4.2). The chirp mismatch parameter $\hat{\alpha}$ estimated in Step 1 is added to (4.3). Through the parametric sweep, the error compensation term h_k is updated and again multiplied with y_k. The range-Doppler image I is generated using K number of range profiles Y_k for given η_1 and γ_1, and the image quality is measured for the range-Doppler image each time while sweeping the error parameters as follows:

$$J_2\ (\eta_1, \gamma_1,) = \mathrm{IQA}\left(\hat{I}(\eta_1, \gamma_1)\right). \tag{17}$$

After the parametric sweep, the error parameters that provide the maximum/highest image quality are selected, as shown in the following equation:

$$\{\hat{\eta_1}, \hat{\gamma_1}\} = \underset{\eta_1,\ \gamma_1\ \in \mathbb{R}}{\arg\max}\ J_2(\eta_1, \gamma_1). \tag{18}$$

For the final image generation, all the estimated error parameters $\hat{\eta_1}$, $\hat{\gamma_1}$, and $\hat{\alpha}$ obtained in Steps 1 and 2 are added to the error compensation term h_k and correct the phase errors in the received signals y_k along the slow time. The range-Doppler image is formed using the error-corrected range profiles $\hat{Y}_k$.

The summary of the semiblind synchronization method is given as follows.

1) Collect N number of pulses/received signals.
2) Sweep parameter α and compute h_k (Step 1).
3) Estimate α from J_1 (Step 1).
4) Sweep parameters η_1 and γ_1 (Step 2).
5) Compute h_k for η_1, γ_1, and $\hat{\alpha}$ (Step 2).
6) Estimate η_1 and γ_1 from J_2 (Step 2).
7) Compensate synchronization errors using the estimated error parameters $\hat{\eta}_1$, $\hat{\gamma}_1$, and $\hat{\alpha}$ (final image generation).
8) Form the final range-Doppler image using the phase-corrected HRRPs (final image generation).

B. Image Quality Metrics

In this study, image quality metrics, including image sharpness (IS), image contrast (IC), and image entropy (IE), are considered and tested for IQA in the semiblind synchronization method. First, the IS is expressed as follows:

$$\mathrm{IS} = \sum_{m=1}^{M}\sum_{n=1}^{N} \Psi\left[I(m,n)\right] \tag{19}$$

where I is the image amplitude and Ψ is a convex function of a nonnegative variable. There are many possible forms to assess IS. The power law function $\Psi(x) = x^{\nu}$ and entropy function $\Psi(x) = x \ln x$ are the most popular forms [23]. In addition, the function $\Psi(x) = -\ln(x+b)$ was introduced for the solution to maximum-likelihood and maximum-posterior estimation problems, where b can be interpreted as the intensity of the background in the prior model for the scene reflectance [24]. In this study, the power law function using $\nu = 2$ is considered for IS.

Next, the IC is considered and tested for the semiblind synchronization method. The IC is defined as follows:

$$\mathrm{IC} = \frac{\sqrt{E\left\{\left[|I| - E(|I|)\right]^2\right\}}}{E(|I|)}. \tag{20}$$

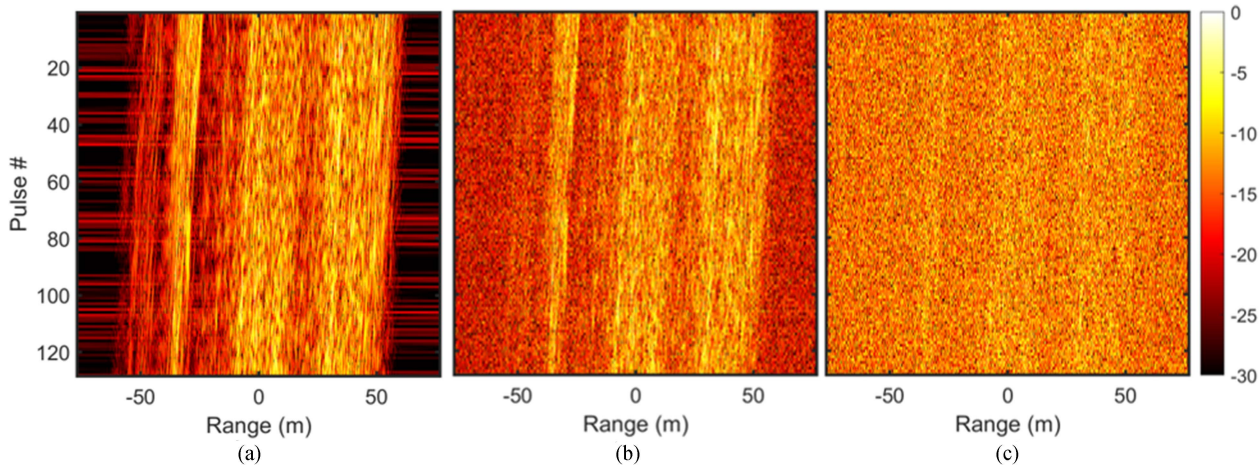

Fig. 7. Range profiles with (a) no-noise, (b) 20-dB SNR, and (c) 10-dB SNR cases.

IC is defined as the ratio of the standard deviation and the mean value of the image intensity. E denotes the spatial mean operator. IC is a popular indicator of image quality [25], [26]. The IC value may depend on the number of reconstructed scatterers. In other words, the images with the fewer number of scatterers tend to have a higher IC value [25], [26].

Finally, the IE is tested. The 1-D entropy and 2-D IE are widely used in range alignment and phase error compensation [27], respectively, for motion compensation. The 2-D IE function of the radar image is defined as follows:

$$\mathrm{IE} = -\sum_{m=1}^{M}\sum_{n=1}^{N} P(m,n)\ln P(m,n) \tag{21}$$

where $P(m,n) = \frac{|I(m,n)|}{\sum_{m=1}^{M}\sum_{n=1}^{N}|I(m,n)|}$ is the power normalized image [27]. A well-focused ISAR image tends to have a low IE value.

C. Simulation Results

Fig. 7 shows the simulated range profiles using the synchronization errors, as discussed in Fig. 5(d). Synchronization errors, which are $\eta_1 = 100\,\mathrm{kHz}$, $\gamma_1 = 1\,\mathrm{ns}$, and $\alpha = 0.9$, are added in the system model to test and validate the LFM-based, semiblind synchronization method. The simulation parameters and rotational motion, as discussed in Section II-B, are used in this simulation study. Fig. 7(a) shows the range profiles from 128 pulses without system noise. The vertical axis is the pulse number. Complex white Gaussian noise was added to the range profiles to simulate signal-to-noise ratio (SNR) of 20 and 10 dB, which are shown in Fig. 7(b) and (c).

The semiblind synchronization method was tested using the simulated data, as shown in Fig. 7. As discussed in Section IV-A, the chirp mismatch parameter α was first estimated as a part of Step 1. Fig. 8 shows the normalized J_1 in (15) to estimate α. α was swept from 0.8 to 1 in this case. Fig. 8(a) and (b) shows the parameter sweep results using IC and IE, respectively. In the figures, the blue solid line is the no-noise case, and the red dash and the black dash lines are the 20- and 10-dB SNR cases.

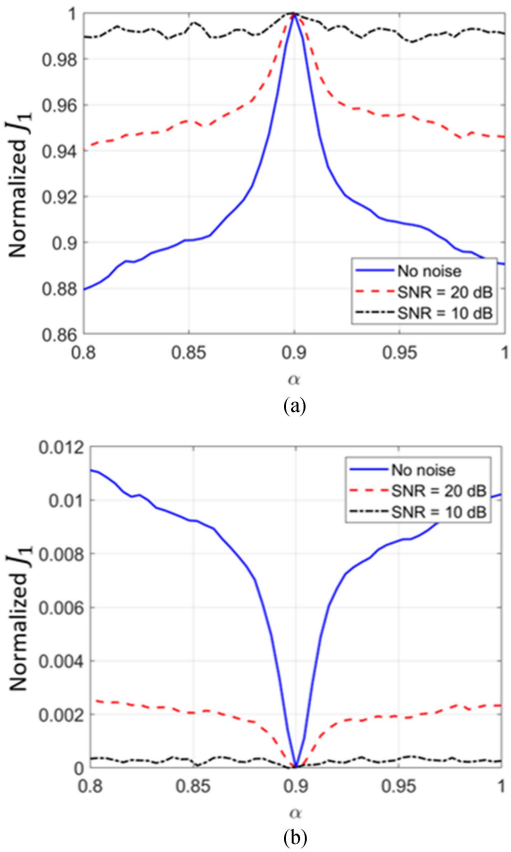

Fig. 8. Estimation of chirp mismatch parameter α using (a) IC and (b) IE.

The simulation results show that both IC and IE can accurately estimate the error parameter, which was $\alpha = 0.9$. In addition, the comparison of no-noise, and 20-dB and 10-dB SNR cases in Fig. 8 indicates that, as noise increases, J_1 becomes less sensitive to α.

Fig. 9 shows an example of Step 2 for estimating frequency drift η_1 and time drift γ_1. Image quality metrics, including IS, IC, and IE, were used in this example. Each parametric sweep map

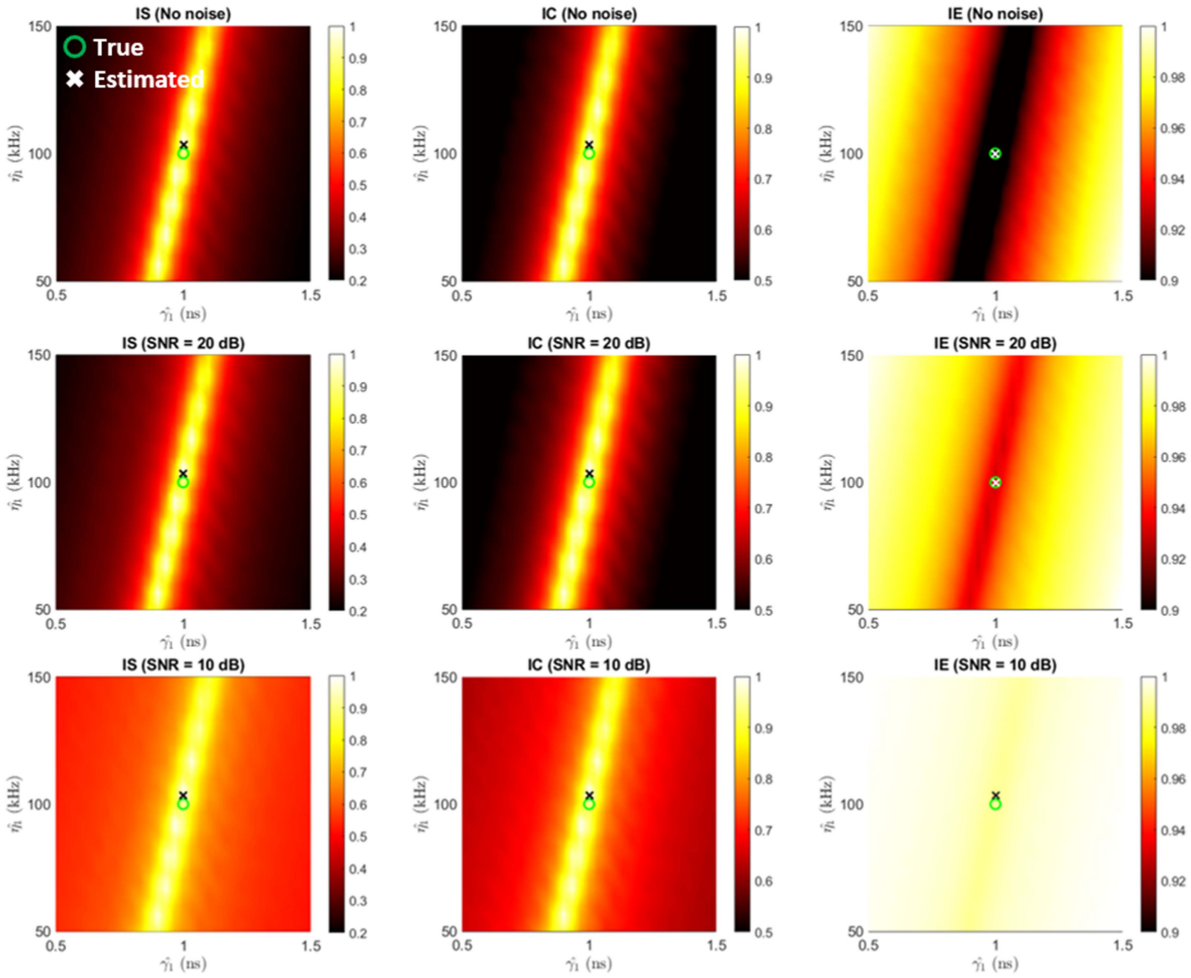

Fig. 9. Frequency η_1 and time γ_1 offset estimation using IQA for no-noise, 20-dB SNR, and 10-dB SNR cases.

in Fig. 9 shows the quantitative values using one of the image quality metrics for no noise, 20-dB SNR, and 10-dB SNR. The map is normalized by its maximum value after the parameter sweep. The comparison of the parametric sweep maps shows that the dynamic range of the maps decreases as noise increases, as shown in Fig. 8. The horizontal and vertical axes represent the error parameters for frequency offset η_1 varied from 50 to 150 kHz and the time offset parameter γ_1 varied from 0.5 to 1.5 ns. We selected 3.33 kHz and 0.033 ns for η_1 and γ_1, respectively. Note that the range of error parameters is assumed to be known via characterization and measurement of the system prior to the system deployment. The green circle marker shows the true error parameters added to the system model, and the cross marker indicates the estimated parameters. The true and estimated errors are closely located in the parametric sweep map. The results indicate that the image quality metrics can be used to estimate the error parameters in Step 2 of the semiblind synchronization method. Fig. 10 shows that the minimum IE point, which indicates $\widehat{\eta_1}$ and $\widehat{\gamma_1}$, is found in the parametric sweep map. In order to find the global minima or maxima value, the range of the parametric sweep must cover the actual error parameters and the step size has to be fine enough to distinguish

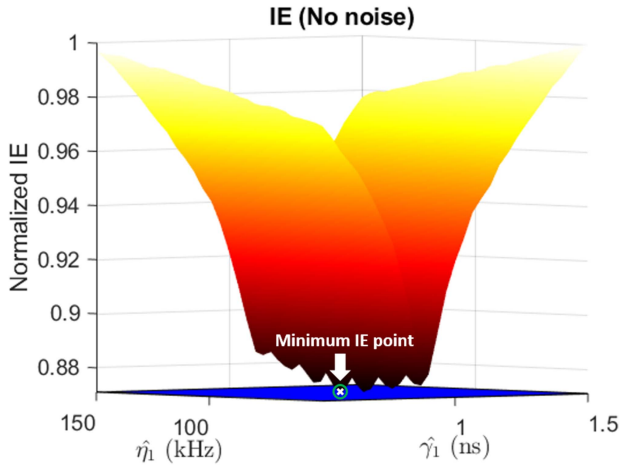

Fig. 10. Parametric sweep map using IE for no noise and the minimum IE point.

the global and the local values. Among the quality metrics, the IE provides the best performance. Fig. 9 (top right) and (center right) images show the parametric sweep map using IE

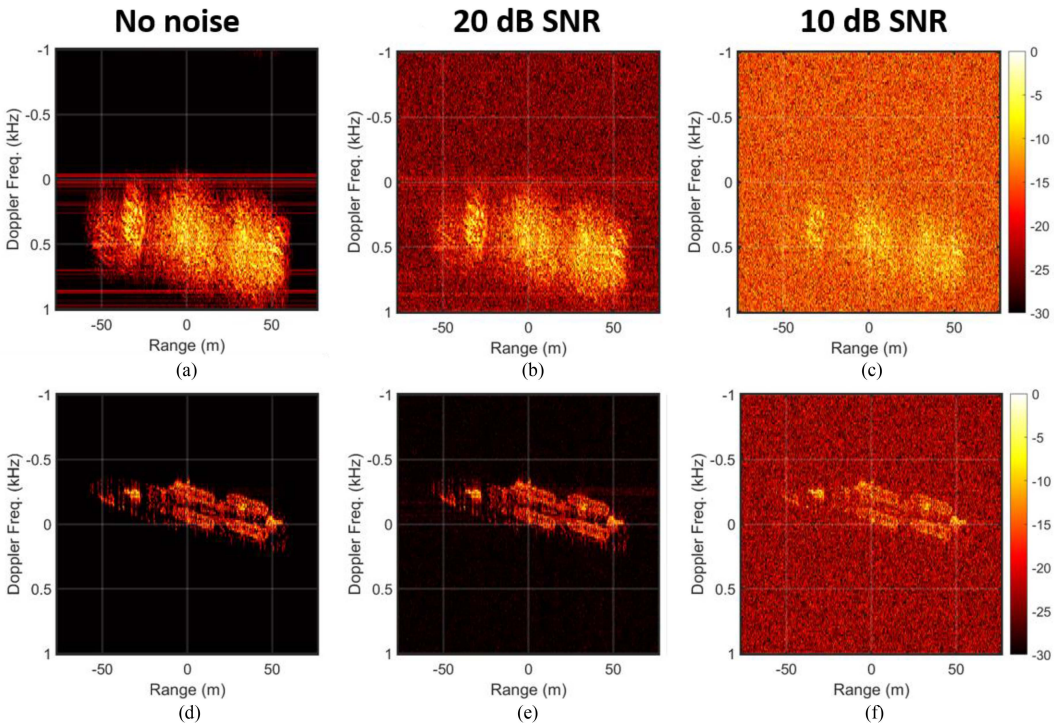

Fig. 11. Range-Doppler images (a–c) before and (d–f) after error compensation for (a and d) no-noise, (b and e) 20-dB SNR, and (c and f) 10-dB SNR cases.

for no-noise (top right) and 20-dB SNR (center right) cases. In these two cases, the true and estimated error parameters were the same.

After error estimation, those estimated error parameters were added in (4) and then (14) to calculate and compensate the phase errors along the pulses. Fig. 11 compares the range-Doppler images before and after error compensation using the estimated parameters obtained from Steps 1 and 2 using IE for no-noise, 20-dB SNR, and 10-dB SNR cases. Fig. 11(a)–(c) shows the range-Doppler images before applying the semiblind synchronization method for no noise, 20-dB SNR, and 10-dB SNR, respectively. The bottom figures show the corresponding images after error compensation using the method. Note that the resulting images are shown as rotated due to the effect of $\Delta\Omega_T$ in ϕ_{b_i}, as discussed in Section III-B. For the error estimation, among the image quality metrices, IE in (21) is used for IQA. The comparison of the resulting images indicates that the noise floor tends to become lower as images are focused better. Fig. 11(d)–(f) shows that the semiblind synchronization method can estimate and compensate the synchronization errors, including chirp rate mismatch, transmitter frequency, and time drift, that are simultaneously added to the received signals. The IE of Fig. 11(a) is $\sim$13% higher than Fig. 4(b), which was generated without any synchronization errors. Using the semiblind synchronization method, we were able to reduce the IE $< 1\%$, which is shown in Fig. 11(d). As a result, range-Doppler processing generated well-focused images, which allows recognition of the boat structures for all the noise cases, including 10-dB SNR in Fig. 11(f).

V. Conclusion

In this article, we introduced a semiblind synchronization scenario and method for bistatic, range-Doppler image processing where conventional synchronization methods are not available or sufficient to maintain coherence between transmitter and receiver. To validate the method, three synchronization errors; and chirp rate mismatch, and time and frequency offsets were analyzed and added to the bistatic system model using an LFM waveform and stretch processing. The simulation study has shown that those errors degrade range resolution and cause scatterer migration, which decreases the overall image quality. The LFM-based, semiblind synchronization method uses a parametric sweep and IQA to estimate the phase contribution of the synchronization errors based on the transmitted waveform structure and received signals. Our simulation results show that the method enables the estimation and compensation of the errors, and refocuses the range-Doppler image without sharing oscillator signals or using direct-path signals. Our semiblind synchronization technique has potentially broad applicability in emerging remote sensing applications, such as for facilitating large-scale Earth observations, using bistatic radar systems.

Appendix

The received signal y_k after down-conversion and the deramping process is

$$y_k\ (u) = \tilde{x}_{\ k}\,(t)\exp\left(-j\left[\Omega_R\,(u-t_0)+\varphi_R\,(u-t_0)\right]\right)$$

$$\exp\left(-j\frac{\pi\boldsymbol{\alpha}\beta}{\tau}(u-t_0)^2\right) \tag{A.1}$$

where $\tilde{x}_k\ (t) = \xi\exp(j\frac{\pi\beta}{\tau}(u-\tilde{t}_b)^2)\exp(j[\Omega_T(u-\tilde{t}_b)+\varphi_T(u-\tilde{t}_b)])$, $u = t+\Delta t$, $\tilde{t}_b = t_b + \Delta t$, and $t_b = t_0 + \Delta t_b$, $0 \le t - t_b \le \tau$. Thus, the expanding terms are

$$\begin{aligned} y_k(u) &= \xi\exp\left(j\frac{\pi\beta}{\tau}(u-\tilde{t}_b)^2\right)\exp\left(-j\frac{\pi\alpha\beta}{\tau}(u-t_0)^2\right) \\ &\quad \exp\left(j[\Omega_T(u-\tilde{t}_b)+\varphi_T(u-\tilde{t}_b)]\right) \\ &\quad \exp\left(-j[\Omega_R(u-t_0)+\varphi_R(u-t_0)]\right). \end{aligned} \tag{A.2}$$

The first two terms of (A.2) can be expressed as

$$\begin{aligned} &\exp\left(j\frac{\pi\beta}{\tau}(u-\tilde{t}_b)^2\right)\exp\left(-j\frac{\pi\boldsymbol{\alpha}\beta}{\tau}(u-t_0)^2\right) \\ &= \exp\left(j\frac{\pi\beta}{\tau}[(u-\tilde{t}_b)^2-\alpha(u-t_0)^2]\right) \\ &= \exp\left(j\frac{\pi\beta}{\tau}\left[u-\tilde{t}_b-\sqrt{\alpha}(u-t_0)\right]\left[u-\tilde{t}_b+\sqrt{\alpha}(u-t_0)\right]\right) \\ &= \exp\left(j\frac{\pi\beta}{\tau}\left[u-\sqrt{\alpha}u+\sqrt{\alpha}t_0-\tilde{t}_b\right]\left[u+\sqrt{\alpha}u-\sqrt{\alpha}t_0-\tilde{t}_b\right]\right) \\ &= \exp\left(j\frac{\pi\beta}{\tau}\left[(1-\sqrt{\alpha})u+\sqrt{\alpha}t_0-t_b-\Delta t\right]\ \left[(1+\sqrt{\alpha})u\right.\right. \\ &\quad \left.\left.-\sqrt{\alpha}t_0-t_b-\Delta t\right]\right) \\ &= \exp\left(j\frac{\pi\beta}{\tau}\left[(1-\sqrt{\alpha})u+\sqrt{\alpha}t_0-t_0-\Delta t_b-\Delta t\right]\left[(1+\sqrt{\alpha})u\right.\right. \\ &\quad \left.\left.-\sqrt{\alpha}t_0-t_0-\Delta t_b-\Delta t\right]\right) \\ &= \exp\left(j\frac{\pi\beta}{\tau}\left[(1-\sqrt{\alpha})(u-t_0)-(\Delta t_b+\Delta t)\right]\left[(1+\sqrt{\alpha})\right.\right. \\ &\quad \left.\left.(u-t_0)-(\Delta t_b+\Delta t)\right]\right) \\ &= \exp\left(j\frac{\pi\beta}{\tau}\left[(1-\sqrt{\alpha})(u-t_0)-\Delta\tilde{t}_b\right]\left[(1+\sqrt{\alpha})(u-t_0)\right.\right. \\ &\quad \left.\left.-\Delta\tilde{t}_b\right]\right). \end{aligned} \tag{A.3}$$

The rest terms can be expressed as

$$\begin{aligned} &\exp\left(j[\Omega_T(u-\tilde{t}_b)+\varphi_T(u-\tilde{t}_b)]\right)\exp\left(-j[\Omega_R(u-t_0)\right. \\ &\left.+\varphi_R(u-t_0)]\right) \\ &= \exp\left(-j(\Omega_R-\Omega_T)u\right)\exp\left(-j\Omega_T\tilde{t}_b+j\Omega_R t_0\right)\ \exp(-j[\\ &\quad \varphi_R(u-t_0)-\varphi_T(u-\tilde{t}_b)]) \\ &= \exp\left(-j\Delta\Omega u\right)\exp\left(-j\Omega_T\tilde{t}_b+j(\Omega_T+\Delta\Omega)t_0\right)\exp(-j[\\ &\quad \varphi_R(u-t_0)-\varphi_T(u-\tilde{t}_b)]) \\ &= \exp\left(-j\Delta\Omega u\right)\exp\left(-j\Omega_T(\tilde{t}_b-t_0)+j\Delta\Omega t_0\right)\exp(-j[\\ &\quad \varphi_R(u-t_0)-\varphi_T(u-\tilde{t}_b)]) \\ &= \exp\left(-j\Delta\Omega(u-t_0)\right)\exp\left(-j\Omega_T(\tilde{t}_b-t_0)\right)\exp(-j[\\ &\quad \varphi_R(u-t_0)-\varphi_T(u-\tilde{t}_b)]) \\ &= \exp\left(-j\Delta\Omega(u-t_0)\right)\exp\left(-j\Omega_T\Delta\tilde{t}_b\right)\exp(-j[\varphi_R(u-t_0) \\ &\quad -\varphi_T(u-\tilde{t}_b)]) \end{aligned} \tag{A.4}$$

where $\Delta\Omega = \Omega_R - \Omega_T = \Delta\Omega_R - \Delta\Omega_T$, $\Omega_T = \Omega_o + \Delta\Omega_T$, and $\Omega_R = \Omega_o + \Delta\Omega_R$.

The received signal y_k can be rewritten using (A.3) and (A.4) as follows:

$$\begin{aligned} y_k(u) = \xi\exp&\left(j\frac{\pi\beta}{\tau}\left[(1-\sqrt{\alpha})(u-t_0)-\Delta\tilde{t}_b\right]\left[(1+\sqrt{\alpha})\right.\right. \\ &\left.\left.(u-t_0)-\Delta\tilde{t}_b\right]\right)\exp\left(-j\Delta\Omega(u-t_0)\right)\exp\left(-j\Omega_T\Delta\tilde{t}_b\right) \\ &\exp\left(-j\left[\varphi_R(u-t_0)-\varphi_T(u-\tilde{t}_b)\right]\right). \end{aligned} \tag{A.5}$$

For N number of scatterers, (A.5) can be expressed as

$$\begin{aligned} y_k(u) &= \sum_{i=1}^{N}\xi_i\exp\left(j\frac{\pi\beta}{\tau}\left[(1-\sqrt{\alpha})(u-t_0)-\Delta\tilde{t}_{b_i}\right]\right. \\ &\left.(1+\sqrt{\alpha})(u-t_0)-\Delta\tilde{t}_{b_i}\right])\exp\left(-j\Delta\Omega(u-t_0)\right) \\ &\times[\exp\left(-j\varphi_T(u-\tilde{t}_{b_i})\right) \\ &\times\exp\left(-j\Omega_T\Delta\tilde{t}_{b_i}\right)\exp\left(-j\left[\varphi_R(u-t_0)-\varphi_T(u-\tilde{t}_{b_i})\right]\right) \\ &= \sum_{i=1}^{N}\xi_i\exp\left(-j\Omega_T(\Delta t_{b_i}+\Delta t)\right)\exp\left(-j\Delta\Omega(u-t_0)\right) \\ &\exp\left(j\frac{\pi\beta}{\tau}(1-\alpha)(u-t_0)^2\right)\exp\left(j\frac{\pi\beta}{\tau}(\Delta\tilde{t}_{b_i})^2\right) \\ &\exp\left(-j\frac{\pi\beta}{\tau}\left[2(u-t_0)\Delta\tilde{t}_{b_i}\right]\right)\exp(-j[\varphi_R(u-t_0) \\ &-\varphi_T(u-\tilde{t}_{b_i})]) \\ &= \exp\left(-j\Omega_T\Delta t\right)\exp\left(-j\Delta\Omega(u-t_0)\right)\exp\left(j\frac{\pi\beta}{\tau}(1-\alpha)\right. \\ &\left.(u-t_0)^2\right)\exp\left(-j\varphi_R(u-t_0)\right)\ \sum_{i=1}^{N}\xi_i\exp(-j\Omega_T \\ &\Delta t_{b_i})\exp\left(j\frac{\pi\beta}{\tau}(\Delta t_{b_i}+\Delta t)^2\right)\exp\left(-j\frac{2\pi\beta}{\tau}(u-t_0)\right. \\ &\times(\Delta t_{b_i}+\Delta t)\exp\left(-j\varphi_T(u-\tilde{t}_{b_i})\right) \\ &= \exp\left(-j\Omega_T\Delta t\right)\exp\left(-j\Delta\Omega(u-t_0)\right)\exp\left(j\frac{\pi\beta}{\tau}(1-\alpha)\right. \\ &\left.\times(u-t_0)^2\right)\exp\left(-j\varphi_R(u-t_0)\right)\exp\left(j\frac{\pi\beta}{\tau}(\Delta t)^2\right) \\ &\exp\left(-j\frac{\pi\beta}{\tau}2(u-t_0)\Delta t\right)\sum_{i=1}^{N}\xi_i\exp\left(-j\Omega_T\Delta t_{b_i}\right) \\ &\exp\left(j\frac{\pi\beta}{\tau}(\Delta t_{b_i})^2\right)\exp\left(j\frac{2\pi\beta}{\tau}\Delta t\Delta t_{b_i}\right)\exp\left(-j\frac{\pi\beta}{\tau}\right. \\ &\left.2(u-t_0)\Delta t_{b_i}\right)\exp\left(-j\varphi_T(u-\tilde{t}_{b_i})\right) \\ &= \exp\left(-j\Omega_T\Delta t\right)\exp\left(-j\Delta\Omega(u-t_0)\right)\exp\left(j\frac{\pi\beta}{\tau}(1-\alpha)\right. \\ &(u-t_0)^2\exp\left(-j\varphi_R(u-t_0)\right)\exp\left(j\frac{\pi\beta}{\tau}(\Delta t)^2\right) \end{aligned}$$

$$\begin{aligned}
&\exp\left(-j\frac{2\pi\beta}{\tau}\left(u-t_0\right)\Delta t\right)\sum_{i=1}^{N}\xi_i\exp(-j\left(\Omega_T-\frac{2\pi\beta}{\tau}\Delta t\right)\\
&\Delta t_{b_i})\exp\left(j\frac{\pi\beta}{\tau}(\Delta t_{b_i})^2\right)\exp\left(-j\frac{2\pi\beta}{\tau}\left(u-t_0\right)\Delta t_{b_i}\right)\\
&\exp\left(-j\varphi_T\left(u-\tilde{t}_{b_i}\right)\right)\\
&=\exp\left(j\phi_\varepsilon\left(u\right)\right)\sum_{i=1}^{N}\xi_i\exp\left(-j\left(\Omega_T-\frac{2\pi\beta}{\tau}\Delta t\right)\Delta t_{b_i}\right)\\
&\exp\left(j\frac{\pi\beta}{\tau}(\Delta t_{b_i})^2\right)\exp\left(-j\frac{2\pi\beta}{\tau}\left(u-t_0\right)\Delta t_{b_i}\right)\\
&\exp\left(-j\varphi_T\left(u-\tilde{t}_{b_i}\right)\right)\\
&=\exp\left(j\phi_\varepsilon\left(u\right)\right)\sum_{i=1}^{N}\xi_i\exp\left(j\phi_{b_i}\left(u\right)\right). \qquad \text{(A.6)}
\end{aligned}$$

The phase error due to the contributions of synchronization errors $\phi_\varepsilon(u)$ is

$$\begin{aligned}
\phi_\varepsilon\left(u\right)=&\left[\frac{\pi\beta}{\tau}\Delta t-\left(\Omega_0+\Delta\Omega_T\right)\right]\Delta t-\left[\frac{2\pi\beta}{\tau}\Delta t\right.\\
&\left.+\left(\Delta\Omega_R-\Delta\Omega_T\right)\right]\left(u-t_0\right)+\frac{\pi\beta}{\tau}\left(1-\alpha\right)\left(u-t_0\right)^2\\
&+\varphi_R\left(u-t_0\right)\\
=&\mathcal{C}_0+\mathcal{C}_1\left(u-t_0\right)+\mathcal{C}_2(u-t_0)^2+\varphi_R\left(u-t_0\right) \qquad \text{(A.7)}
\end{aligned}$$

where $\mathcal{C}_0=[\frac{\pi\beta}{\tau}\Delta t-(\Omega_0+\Delta\Omega_T)]\Delta t, \mathcal{C}_1=-[\frac{2\pi\beta}{\tau}\Delta t+(\Delta\Omega_R-\Delta\Omega_T)]$, and $\mathcal{C}_2=\frac{\pi\beta}{\tau}\left(1-\alpha\right)$. The phase of scattering responses $\phi_{b_i}(t)$ is

$$\begin{aligned}
\phi_{b_i}\left(t\right)=&-\left(\Omega_T-\frac{2\pi\beta}{\tau}\Delta t\right)\Delta t_{b_i}+\frac{\pi\beta}{\tau}(\Delta t_{b_i})^2-\frac{2\pi\beta}{\tau}\\
&\times\left(u-t_0\right)\Delta t_{b_i}-\varphi_T\left(u-t_{b_i}-\Delta t\right)\\
=&-\frac{2\pi\beta}{\tau}\Delta t_{b_i}\left(t+\Delta t-\mathrm{t}_0\right)-\left[\left(\Omega_0+\Delta\Omega_T\right)-\frac{2\pi\beta}{\tau}\Delta t\right]\\
&\times\Delta t_{b_i}+\frac{\pi\beta}{\tau}(\Delta t_{b_i})^2-\varphi_T\left(u-t_{b_i}-\Delta t\right)\\
=&-\frac{2\pi\beta}{\tau}\Delta t_{b_i}t-\theta \qquad \text{(A.8)}
\end{aligned}$$

where $\theta=[(\Omega_0+\Delta\Omega_T)-\frac{2\pi\beta}{\tau}\Delta t]\Delta t_{b_i}+\frac{\pi\beta}{\tau}(\Delta t_{b_i})^2+\frac{2\pi\beta}{\tau}\Delta t_{b_i}(\Delta t-t_0)-\varphi_T(u-t_{b_i}-\Delta t)=[(\Omega_0+\Delta\Omega_T)-\frac{2\pi\beta}{\tau}t_0]\Delta t_{b_i}+\frac{\pi\beta}{\tau}(\Delta t_{b_i})^2-\varphi_T(u-t_{b_i}-\Delta t)$.

REFERENCES

[1] E. Raines, J. Park, J. T. Johnson, and R. J. Burkholder, "A comparison of bistatic and monostatic radar images of 1-D perfectly conducting rough surfaces," *IEEE Geosci. Remote Sens. Lett.*, vol. 19, pp. 1–5, 2022, Art. no. 3508105, doi: 10.1109/LGRS.2021.3104593.

[2] M. Weib, "Synchronisation of bistatic radar systems," in *Proc. IEEE Int. Geosci. Remote Sens. Symp.*, 2004, pp. 1750–1753.

[3] G. Krieger and M. Younis, "Impact of oscillator noise in bistatic and multistatic SAR," *IEEE Geosci. Remote Sens. Lett.*, vol. 3, no. 3, pp. 424–428, Jul. 2006.

[4] M. Martorella, "Analysis of the robustness of bistatic inverse synthetic aperture radar in the presence of phase synchronisation errors," *IEEE Trans. Aerosp. Electron. Syst.*, vol. 47, no. 4, pp. 2673–2689, Oct. 2011.

[5] M. Martorella, J. Palmer, J. Homer, B. Littleton, and I. D. Longstaff, "On bistatic inverse synthetic aperture radar," *IEEE Trans. Aerosp. Electron. Syst.*, vol. 43, no. 3, pp. 1125–1134, Jul. 2007.

[6] J. Park and R. G. Raj, "Impact of synchronization errors in stretch processing for ultra-wideband bistatic radar imaging," in *Proc. IEEE Geosci. Remote Sens. Symp.*, 2023, pp. 356–359.

[7] W.-Q. Wang and D. Jiang, "Integrated wireless sensor systems via nearspace and satellite platforms: A review," *IEEE Sensors J.*, vol. 14, no. 11, pp. 3903–3914, Nov. 2014.

[8] W. Q. Wang, X. D. Liang, and C. B. Ding, "Time and phase synchronisation via direct-path signal for bistatic synthetic aperture radar systems," *IET Radar, Sonar Navig.*, vol. 2, no. 1, pp. 1–11, Feb. 2008.

[9] J. Tian, Y. Chen, N. Xie, and D. Hou, "Bistatic ISAR imaging based on phase synchronization with fiber optic link," in *Proc. IEEE Radar Conf.*, 2016, pp. 1–5.

[10] M. Eineder, "Oscillator clock drift compensation in bistatic interferometric SAR," in *Proc. IEEE Int. Geosci. Remote Sens. Symp.*, 2003, pp. 1449–1451.

[11] S. Prager, M. S. Haynes, and M. Moghaddam, "Wireless subnanosecond RF synchronization for distributed ultrawideband software-defined radar networks," *IEEE Trans. Microw. Theory Techn.*, vol. 68, no. 11, pp. 4787–4804, Nov. 2020.

[12] M. Younis, R. Metzig, and G. Krieger, "Performance prediction of a phase synchronization link for bistatic SAR," *IEEE Geosci. Remote Sens. Lett.*, vol. 3, no. 3, pp. 429–433, Jul. 2006.

[13] W.-Q. Wang, "GPS-based time and phase synchronization processing for distributed SAR," *IEEE Trans. Aerosp. Electron. Syst.*, vol. 45, no. 3, pp. 1040–1051, Jul. 2009.

[14] Y. Chen, W. Tian, L. Yin, and J. Wang, "Integrated time-frequency synchronisation method for cooperative bistatic radar," in *Proc. IET Int. Radar Conf.*, vol. 2019, no. 19, 2019 pp. 6008–6011.

[15] P. J. Beasley and M. A. Ritchie, "Multistatic radar synchronisation using COTS GPS disciplined oscillators," in *Proc. Int. Conf. Radar Syst.*, 2022, pp. 429–434.

[16] K. S. Kulpa and J. Misiurewicz, "Stretch processing for long integration time passive covert radar," in *Proc. CIE Int. Conf. Radar*, 2006, pp. 1–4.

[17] J. V. Eshbaugh, R. L. Morrison, E. W. Hoen, T. C. Hiett, and G. R. Benitz, "HUSIR signal processing," *Lincoln Lab. J.*, vol. 21, no. 1, pp. 115–134, 2014.

[18] M. A. Richards, *Fundamentals of Radar Signal Processing*, 3rd ed. New York, NY, USA: McGraw Hill, 2022.

[19] B. M. Keel and M. Baden, "Advanced pulse compression waveform modulations and techniques," in *Principles of Modern Radar: Advanced Techniques*. Rijeka, Croatia: SciTech Publishing, 2012, pp. 19–85.

[20] V. C. Chen and M. Martorella, *Inverse Synthetic Aperture Radar Imaging: Principles, Algorithms and Applications*. Rijeka, Croatia: SciTech Publishing, 2014.

[21] M. A. Weiss, in *Proc. Workshop Synchronization Timing Syst. Tut. Session [PDF document]*, 2021. [Online]. Available: Available in https://wsts.atis.org/wp-content/uploads/2021/03/01_Tutorial_Atomic_Clocks_and_PRS_slides_with_extras_MWeiss_.pdf

[22] H. Y. Kim, "Modeling and tracking time-varying clock drifts in wireless networks," Ph.D. dissertation, School of Elect. Comput. Eng., Georgia Inst. of Technol., Atlanta, GA, USA, Aug. 2014.

[23] Y. Gao, W. Yu, Y. Liu, R. Wang, and C. Shi, "Sharpness-based autofocusing for stripmap SAR using an adaptive-order polynomial model," *IEEE Geosci. Remote Sens. Lett.*, vol. 11, no. 6, pp. 1086–1090, Jun. 2014.

[24] T. J. Schulz, "Optimal sharpness function for SAR autofocus," *IEEE Signal Process. Lett.*, vol. 14, no. 1, pp. 27–30, Jan. 2007.

[25] M. Martorella, F. Berizzi, and B. Haywood, "Contract maximisation based technique for 2-D ISAR autofocusing," *IEE Proc.-Radar, Sonar Navig.*, vol. 152, no. 4, pp. 253–262, Aug. 2005.

[26] F. Berizzi and G. Corsini, "Autofocusing of inverse synthetic aperture radar images using contrast optimization," *IEEE Trans. Aerosp. Electron. Syst.*, vol. 32, no. 3, pp. 1185–1191, Jul. 1996.

[27] L. Xi, L. Guiosui, and J. Ni, "Autofocusing of ISAR images based on entropy minimization," *IEEE Trans. Aerosp. Electron. Syst.*, vol. 35, no. 4, pp. 1240–1252, Oct. 1999.

James Park (Member, IEEE) received the B.S. degree in electronics engineering from KonKuk University, Seoul, South Korea, in 2007, and the M.S. and Ph.D. degrees in electrical and computer engineering from Ohio State University, Columbus, OH, USA, in 2011 and 2012, respectively.

From 2013 to 2020, he was a Research Electronics Engineer with Air Force Research Laboratory, Sensors Directorate, Wright-Patterson AFB, Dayton, OH, USA, where he led several DoD-funded projects and teams. Since 2020, he has been with Radar Division, U.S. Naval Research Laboratory, Washington, DC, USA, where he is currently a Senior Electronics Engineer. He has more than 40 publications in various journals, conferences, and technical reports. His research interests include signal and image processing for advanced radar and microwave remote sensing.

Raghu G. Raj (Senior Member, IEEE) received the undergraduate degrees in computer science and in electrical engineering from Washington University in St. Louis, St. Louis, MO, USA, in 1998, and the M.S. and Ph.D. degrees in electrical engineering from The University of Texas at Austin, Austin, TX, USA, in 2000 and 2007, respectively.

From 2000 to 2004, he was a Communication Systems Engineer with Motorola Inc., Austin. He is currently a Senior Research Scientist and the Head of Radar Imaging and Target ID Section, Radar Division, U.S. Naval Research Laboratory (NRL), Washington, DC, USA, where he leads the research and development of advanced methods in radar imaging, detection, and target identification with applications to various U.S. DoD funded programs. He has authored or coauthored more than 80 publications in various international journals, conferences, and technical reports, and holds nine U.S. patents. His research interests span various signal/image processing, machine learning, and electromagnetic and inverse problems in radar and remote sensing.

Dr. Raj is the Co-Chair of the IEEE SPS SAR Standardization Committee. He was the recipient of the NRL Alan Berman Publication Award.